

ARTICLE

DOI: 10.1038/s41467-017-01993-4

OPEN

# Optical charge state control of spin defects in 4H-SiC

Gary Wolfowicz<sup>1,2</sup>, Christopher P. Anderson<sup>1,3</sup>, Andrew L. Yeats<sup>1,4</sup>, Samuel J. Whiteley<sup>1,3</sup>, Jens Niklas<sup>5</sup>, Oleg G. Poluektov<sup>5</sup>, F. Joseph Heremans<sup>1,4</sup> & David D. Awschalom<sup>1,4</sup>

Defects in silicon carbide (SiC) have emerged as a favorable platform for optically active spin-based quantum technologies. Spin qubits exist in specific charge states of these defects, where the ability to control these states can provide enhanced spin-dependent readout and long-term charge stability. We investigate this charge state control for two major spin qubits in 4H-SiC, the divacancy and silicon vacancy, obtaining bidirectional optical charge conversion between the bright and dark states of these defects. We measure increased photoluminescence from divacancy ensembles by up to three orders of magnitude using near-ultraviolet excitation, depending on the substrate, and without degrading the electron spin coherence time. This charge conversion remains stable for hours at cryogenic temperatures, allowing spatial and persistent patterning of the charge state populations. We develop a comprehensive model of the defects and optical processes involved, offering a strong basis to improve material design and to develop quantum applications in SiC.

<sup>1</sup>Institute for Molecular Engineering, University of Chicago, Chicago, IL 60637, USA. <sup>2</sup>WPI-Advanced Institute for Materials Research (WPI-AIMR), Tohoku University, Sendai, 980-8577, Japan. <sup>3</sup>Department of Physics, University of Chicago, Chicago, IL 60637, USA. <sup>4</sup>Institute for Molecular Engineering and Materials Science Division, Argonne National Laboratory, Lemont, IL 60439, USA. <sup>5</sup>Chemical Sciences and Engineering Division, Argonne National Laboratory, Lemont, IL 60439, USA. Correspondence and requests for materials should be addressed to D.D.A. (email: [awsch@uchicago.edu](mailto:awsch@uchicago.edu))

Optically active color centers in wide bandgap semiconductors have shown considerable potential for a variety of spin-based quantum technologies, from quantum computing and quantum memories<sup>1</sup> to nano-scale sensing<sup>2–4</sup>. Spin defects in silicon carbide (SiC) in particular combine the optical properties required for single-spin measurements<sup>5–10</sup> with wafer-scale growth and silicon-like fabrication capabilities developed for high-power electronics. However, optimizing these systems for spin qubit applications requires an understanding of not only their spin and optical properties, as demonstrated in the negatively charged silicon vacancy ( $V_{Si}^-$ )<sup>5, 11</sup> and the neutral divacancy ( $VV^0$ )<sup>10, 12–14</sup>, but also an understanding of their charge properties.

Impurities in SiC and their charge states have been investigated for conventional electronics applications, as they play an important role in transport properties and in carrier compensation. Most studies involve deep level transient spectroscopy (DLTS)<sup>15, 16</sup>, electron spin resonance (ESR)<sup>17, 18</sup> and density functional theory (DFT)<sup>19–21</sup> with a strong focus on the carbon vacancy ( $V_C$ )<sup>16, 22, 23</sup>, fewer works have addressed  $V_{Si}$  and  $VV$  defects<sup>24</sup>. For the purpose of quantum information, it is desirable to understand the complete physics of the defects themselves, not just their influence on transport or other electrical characteristics of the substrate.

Here we investigate the effect of optical illumination on the stability of the relevant (optically bright) charge states of  $VV$  and  $V_{Si}$ , the ability to control and convert these states between different charge levels, and the implications for quantum applications. We investigate these questions using a combination of techniques including photoluminescence (PL), optically detected magnetic resonance (ODMR) and electron spin resonance (ESR). The  $VV$  and  $V_{Si}$  charge states are both stabilized to the  $VV^0$  and  $V_{Si}^-$  states required to observe PL, whose intensity can be enhanced by up to three orders of magnitude depending on the material (local defect concentrations and Fermi level). For  $VV$  in particular, we observe bidirectional charge conversion between the neutral (bright qubit state) and a dark charge state using mainly near-ultraviolet (365–405 nm) and near-infrared (976 nm) light. This charge conversion is stable at cryogenic temperature and does not affect the ODMR contrast nor the electron spin coherence time, and can therefore be readily applied to increase PL emission from ensembles.

Charge state conversion can have multiple origins, including one-photon and two-photon ionization, free carrier recombination, and charge transfer between defects. In order to fully understand the involved processes, we measure the charge dynamics of  $VV$ ,  $V_{Si}$  and nitrogen (N) under illumination, where N is the main dopant in our semi-insulating 4H-SiC samples. Excitation dependence with wavelengths ranging from 365 to 1310 nm were measured and simulated, offering a comprehensive picture of charge transfer between these defects. In particular, this allows us to identify  $VV^-$  as being the possible dark charge state of the divacancy, while  $V_{Si}^-$  most likely converts to the dark  $V_{Si}^0$  charge state with above-bandgap light.

Control and understanding of these charge dynamics is crucial for maximizing spin qubit readout, choosing adequate background impurity concentrations in samples and optimizing designs of SiC nano-devices for quantum applications. Such methods have also been applied in the nitrogen-vacancy (NV) center in diamond for quantum optics applications<sup>25</sup>, enabling for example reduced spectral diffusion<sup>26</sup> or Stark tuning of the optical transitions through photo excitation of trapped charges<sup>27</sup>. More exotic applications of charge dynamics include high density data storage<sup>28</sup>, STED super-resolution imaging<sup>29, 30</sup> and charge quantum buses<sup>31</sup>.

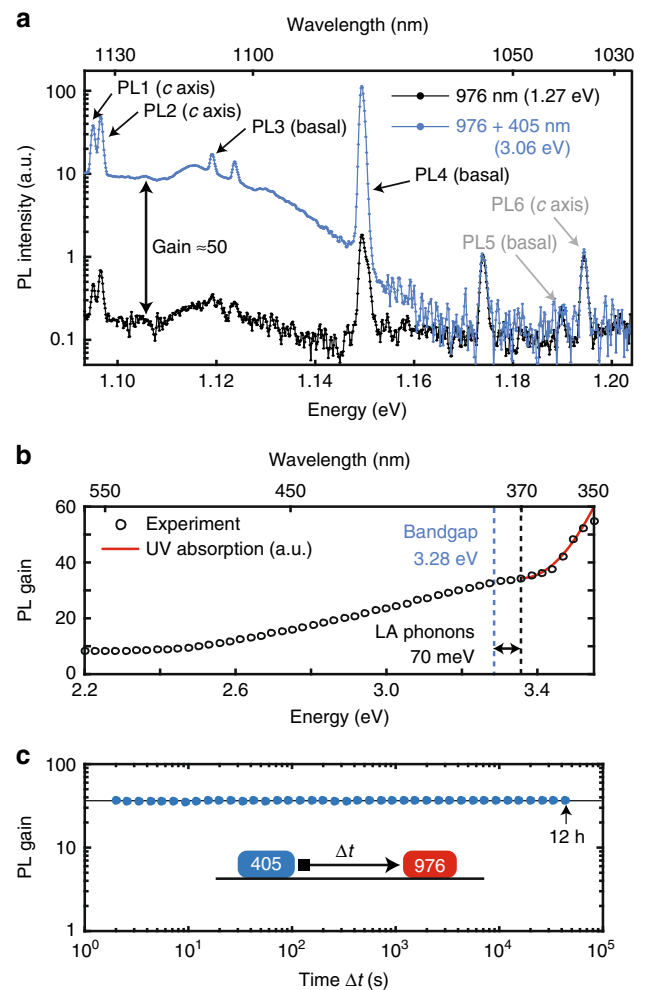


**Fig. 1** Effect of near-bandgap illumination on 4H-SiC divacancies. **a** PL spectrum with 976 nm excitation of the various divacancies in 4H-SiC, as designated in ref. 6, without and with continuous illumination at 405 nm ( $\approx 5$  mW optical power). All the observed PL lines except PL5 and PL6 are enhanced by the UV excitation, including both *c* axis and basal defects. **b** Gain in the PL signal (integrated across PL1–4) as a function of excitation wavelength (energy) around the 4H-SiC bandgap (3.28 eV at 5 K<sup>49</sup>). Power was normalized to 0.4  $\mu$ W across the entire energy range. The onset of change in the curve is shifted from the bandgap energy due to absorption of longitudinal acoustic phonons (about 70–80 meV). The UV absorption and corresponding electron-hole generation rate follows the curve in red, as given in ref. 49. **c** Lifetime of the  $VV^0$  charge state after a 405 nm pulse at 6 K. No significant decay (standard deviation of signal is 2%) is observed after 12 h

## Results

**PL enhancement of  $VV^0$  using UV illumination.** We initially observe a drastic increase in PL intensity of  $VV^0$ , by about 50 times at 6 K, when continuously illuminating a semi-insulating 4H-SiC sample with a 405 nm (“UV”) laser diode, in addition to the 976 nm (1.27 eV) laser required for PL excitation. This is shown in Fig. 1a where the full PL spectrum for all the divacancies (PL1–PL6<sup>6</sup>) is taken with (blue) and without (black) 405 nm (3.06 eV) excitation. Both *c* axis (PL1, PL2) and basal defects (PL3, PL4) show an increase in their PL intensity, with slight variation between defects, which we ascribe to charge conversion of the divacancy toward its observable neutral state. On the other hand, PL5 and PL6 remain completely unaffected, adding another unique feature to these currently unidentified defects on top of

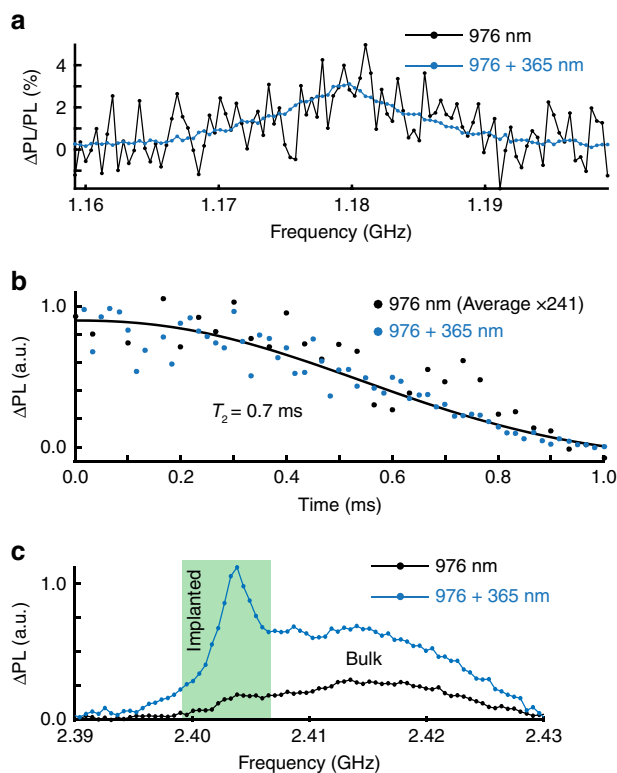


**Fig. 2** Charge conversion effect on the spin properties. ODMR signals are given as relative photoluminescence intensities ( $\Delta\text{PL}$ ) under microwave excitation. **a** CW-ODMR spectrum at 50 G and measured through a monochromator at the 1130.6 nm PL2 zero-phonon line to ensure no other contribution in the optical signal. The intensity is given as the ratio (i.e., contrast) between the ODMR and PL intensity, which remains constant with and without 365 nm illumination, indicating unchanged spin polarization and readout mechanisms. **b** Hahn echo decay experiment for PL2 at  $\approx 400$  G, measured with pulsed-ODMR at 6 K. The 365 nm excitation is continuous throughout the sequence, resulting in a signal increase while the coherence time is unaffected. Decay with 976 nm excitation only was averaged 241 times more than the decay with also 365 nm illumination. Line (in black) is a stretched exponential fit (stretch factor  $\approx 2$ ) to the data. **c** CW-ODMR (PL2 at  $\approx 400$  G) of a 4H-SiC sample with a 500 nm carbon-implant layer below the surface. The divacancies created at the layer are barely visible before 365 nm excitation. The implanted layer peak is also shifted from the bulk due to a magnetic field gradient across the sample

their strong room temperature PL emission. The  $\text{VV}^0$  PL enhancement with UV was observed in all semi-insulating wafers we measured, with gains ranging by a factor of 2–1000 (Supplementary Fig. 2), including samples obtained from separate commercial suppliers (Cree or Norstel), different growth batches, or even simply from separate positions within the same wafer. This strongly indicates an influence from the local environment, e.g., from the remaining concentration of N dopants or other impurities which is known to locally differ in as-grown wafers<sup>32</sup>. The PL intensity with UV remains fairly constant however from sample to sample.

In order to understand the effect of 405 nm illumination, and optimize the enhancement, the excitation wavelength is swept across the 4H-SiC bandgap energy (3.28 eV, 380 nm) as shown in Fig. 1b. The PL gain slowly increases with excitation energy, and around 3.33–3.35 eV, slightly above the 4H-SiC bandgap (3.28 eV), it drastically turns up. This suggests two separate processes are altering the VV charge state from either  $\text{VV}^-$  or

$\text{VV}^+$  to  $\text{VV}^0$ : at low energies, we will see this is due to direct photoionization, while at high energies, the gain results from capture of photo-generated carriers.

We now consider charge dynamics under illumination, starting from the stability of the conversion observed after UV excitation. As illustrated in Fig. 1c, the system is initially pumped with 405 nm toward a high  $\text{VV}^0$  population (strong PL intensity), followed by a long delay to allow for relaxation and finally measurement using 976 nm. No change is observed over the course of 12 h, a result largely expected for a deep defect at cryogenic temperature (6 K). More interestingly, the PL intensity always drops to a low level after turning off the UV excitation while 976 nm was continuously on. Combined with this long stability, this implies that the use of 976 nm to excite VV PL is simultaneously converting the VV out of its neutral-charge state, toward a dark state (more details are given later on). This has significant consequences as wavelengths near 976 nm have been extensively used in recent PL- and ODMR-related works<sup>8, 33, 34</sup>, owing to being close to the absorption maximum of the ground to excited state transition of  $\text{VV}^0$ , as well as being easily available commercially. These previous studies may therefore have been partially perturbed by charge conversion.

**Illumination effects on  $\text{VV}^0$  spin properties.** Above-bandgap excitation can be used to efficiently convert VV toward its neutral-charge state, and more importantly drastically increases the PL intensity. For practical applications, however, we verify this has no effect on the spin properties of  $\text{VV}^0$ . In Fig. 2a, we first measure the ODMR contrast of PL2 at 50 G, i.e., the ratio of ODMR over PL intensity, which provides a direct measure of how the spin states may be affected during illumination. For these experiments, the 405 nm laser is replaced by a 365 nm (also called “UV”) light-emitting diode which is more efficient at charge conversion since it is above bandgap in energy. No difference in contrast is observed with or without 365 nm, and the charge conversion therefore does not significantly affect the spin state nor the readout mechanism. However, the signal-to-noise ratio improves by  $\sim 70$  times with illumination due to increased  $\text{VV}^0$  charge population. More details are given in the Supplementary Fig. 6, Supplementary Note 2 regarding the ODMR experiments presented here.

A second crucial property is the electron spin coherence of the defect. From Fig. 1c, the charge stability at cryogenic temperature (6 K) is shown to be much longer than any coherence timescale<sup>34</sup>; however, we check that even with constant 365 nm illumination ( $\sim 0.2$  mW) and corresponding electron-hole pair generation, the coherence time remains unaffected. At 400 G, the ensemble electron spin coherence  $T_2$  is measured to be 0.7 ms and remains completely unaffected by either light or free carriers (Fig. 2b), while much longer averaging ( $> \times 200$ ) was required to obtain similar signal-to-noise ratios without 365 nm illumination. This is not an obvious result as scattering or exchange interaction with free carriers can easily reduce  $T_1$  or  $T_2$  of defect spins<sup>35</sup>.

Until now, all measurements were realized on as-grown commercial wafers with naturally occurring impurity concentrations. However, carbon ion implantation or electron irradiation<sup>14</sup> is often used to increase the PL intensity and to improve spatial resolution. The type of defects created by lattice damage during these processes cannot be well controlled, though it may be partially managed by annealing, and the local Fermi level may shift away from the desired charge state. We test this with a 500 nm thick layer of implanted divacancies (Methods section). When measuring the PL2 ODMR spectrum of this sample (at  $\approx 400$  G), as shown in Fig. 2c, we obtain a broad “bulk” signal observable across the entire sample depth using simply 976 nm excitation.

When 365 nm is turned on (with constant absorption over the sample depth), the bulk intensity increases as expected, but more importantly a narrower and more intense peak appears. The latter is assigned to the implanted layer which, being confined in depth, is less sensitive to inhomogeneity in the static magnetic field. Rabi experiments at the peak layer frequency yielded as expected an increased contrast (Supplementary Fig. 7), demonstrating that the UV charge stabilization can be critical in such samples.

**VV charge state conversion.** We now consider in more depth the charge mechanisms within 4H-SiC, in particular the effect of 976 nm illumination which appears to convert VV toward a dark charge state ( $VV^-$  or  $VV^+$ ). Since 976 nm is used both for PL excitation and causes charge conversion, it is necessary to separate the two contributions from the PL intensity, which can be achieved by looking at the conversion dynamics under pulsed light. This is realized using a three-pulse scheme: reset with either 976 or 365 nm, pump with a wavelength ranging from 365 to 1310 nm using various laser diodes, and measurement with 976 nm. Typical decay curves as a function of pumping duration are shown in Fig. 3a with different initial reset lasers, pump wavelength, pump power and temperatures.

In Fig. 3b, fitted steady states and decay rates (see Methods section regarding the fitting) are plotted as a function of pump excitation wavelength. Steady-state intensities are all normalized by the steady-state PL intensity after UV pumping. A clear transition is observed between 940 and 976 nm, at about 1.3 eV, for both steady-state values and decay rates, with shorter wavelengths being increasingly more efficient at charge conversion toward  $VV^0$ . In addition, we measure a single wavelength at 1310 nm (0.95 eV) that tentatively suggests a second transition (between 976 and 1310 nm), where the  $VV^0$  charge state becomes insensitive to excitation (no observed decay).

The wavelength transitions can be related to photoionization energies and, though the Franck–Condon shift is unknown here, to formation energies obtained from DFT calculations<sup>20, 36</sup> and reproduced in Fig. 3c. The divacancy defect in 4H-SiC has four stable charge states: +, 0, – and 2–. The (+/0) and (0/–) transition levels are calculated to be, respectively,  $\sim E_v + 1$  eV and  $\sim E_c - 1.1$  eV, with  $E_v$  and  $E_c$  the valence and conduction band energies. On the one hand, these energies correspond closely to ionization from either  $VV^+$  or  $VV^-$  (dark) to  $VV^0$  (bright), and therefore to the observed 1.3 eV optical transition. On the other hand, the minimum energy to photoionize  $VV^0$  to the dark state will be around 2 eV, requiring a two-photon absorption mechanism using 976 nm illumination.  $VV^0$  can absorb one photon to reach its excited state followed by a second photon to ionize either to  $VV^+$  or to  $VV^-$  (Supplementary Fig. 5). As two-photon absorption requires at least the ZPL energy ( $\sim 1.1$  eV, PL1–PL4) to reach the excited state, we expect no decay from  $VV^0$  should occur below this energy as was observed using 1310 nm illumination.

Both  $VV^-$  and  $VV^+$  are candidates for the dark VV charge state, however,  $VV^-$  is more likely from our results. Our semi-insulating samples are compensated N-type samples with nitrogen (N) as primary dopant and carbon vacancies ( $V_C$ ) for compensation. Both species have states lying close to the conduction band (Supplementary Fig. 4). After UV illumination, free electrons will easily be recaptured by N (Fig. 4c) and possibly  $V_C$ , allowing free holes to convert VV from  $VV^-$  to  $VV^0$ . In the following sections we assume that  $VV^-$  is the dark state, though additional studies will be needed to fully resolve this question. It should be mentioned that during review of this paper we became aware of a similar work<sup>37</sup> on optical charge conversion of divacancies in 4H-SiC that hypothesizes  $VV^+$  instead of  $VV^-$ .

We attempt to model the observed dynamics using the rate-equation model shown in Fig. 3d, based on charge transfer between the divacancy and a trap of unknown origin. More details are given in both the Methods section and Supplementary Note 1. Simulated decays and their corresponding rates and steady states are shown in Fig. 3a, b. Three experimental characteristics are nicely reproduced by the model here: (i) the jump in charge conversion efficiency for above bandgap illumination, (ii) the  $VV^-$  to  $VV^0$  transition fitted to be 1.295 (5) eV, and (iii) the  $VV^0$  to  $VV^-$  transition set at the ZPL energy (1.1 eV).

Finally, a temperature dependence of 976 nm pumping (365 nm reset) is taken between 5.5 and 210 K, with corresponding steady-states value shown in Fig. 3e. Above 100 K, the effect of 976 nm pumping compared to 365 nm pumping is drastically reduced. The simulation is able to reproduce this feature owing to thermal electron-hole generation, with possible origins being the thermal emission of shallow defects, such as nitrogen ( $\approx 0.05$ – $0.1$  eV) and boron ( $\approx 0.3$  eV), capture barriers or changes in carrier lifetimes. From the simulation fit, this process has a characteristic activation energy around 0.1–0.2 eV depending on the fit dataset.

In summary, we identify a sharp transition of the VV charge dynamics at around 1.3 eV (960 nm), likely corresponding to the ionization of  $VV^-$  to  $VV^0$ . Below 1.3 eV in energy, two-photon absorption drives the charge state toward  $VV^-$ , while above, VV is preferentially in  $VV^0$  and remains stable for many hours after illumination. In addition, UV light above bandgap strongly drives the system toward  $VV^0$ .

**Charge transfer between major defects.** The experiments described previously made use of PL as a direct measurement of the divacancy neutral-charge state, combined with photo excitation to probe relevant energy levels as well as trapping or recombination dynamics. However, understanding all the major defects in 4H-SiC, not just the divacancy, is required to obtain a comprehensive picture of the sample behavior under illumination. While PL of  $V_{Si}$  can be measured, other important spin impurities, such as  $V_C$  or N are not photo-active, with no optical excited states in the bandgap. We thus turn toward electron spin resonance (ESR) to provide information on all the spin species.

A CW-ESR spectrum at X-band is shown in Fig. 4a with resonance peaks from PL1 to PL4 VV defect types, as well as a cluster of signals near the g-factor  $g=2$ , known to be from  $V_{Si}$ ,  $V_C$  and/or N<sup>13, 18</sup>. In order to properly resolve some of these peaks, we subtract the ESR spectrum measured with 976 nm illumination from the spectrum obtained with either 940 or 365 nm illumination. The differential spectra, shown in Fig. 4b, then correspond to possible charge transfer with VV which is extremely sensitive to these wavelengths (further considerations are discussed in Methods section). The ESR peak intensities are given for the main identified defects in Fig. 4c (left). With 940 nm, two sets of resonances can be clearly assigned, the strongest due to  $V_{Si}^-$  ( $T_{V2a}$  or V2 center) and the weakest from  $N^-$  (k site). At this wavelength,  $VV^-$  undergoes photoionization to become  $VV^0$ , emitting an electron to the conduction band which is likely captured by  $V_{Si}^0$ , and resulting in an increase in  $V_{Si}^-$ . With 365 nm, large changes can be seen around  $g=2$ , possibly from free electrons and  $V_C$ , though the peaks are too clustered to be resolved. On the side of  $g=2$ ,  $N^-$  appears much stronger while the  $V_{Si}^-$  peaks completely disappeared. While this may be due to carrier-induced spin relaxation, such behavior is also well explained by charge dynamics: N, initially in its neutral-charge state due to either photoionization or thermal emission (shallow donor) before cooling down the sample, captures most of the generated electrons to give a high  $N^-$  signal. The holes now in

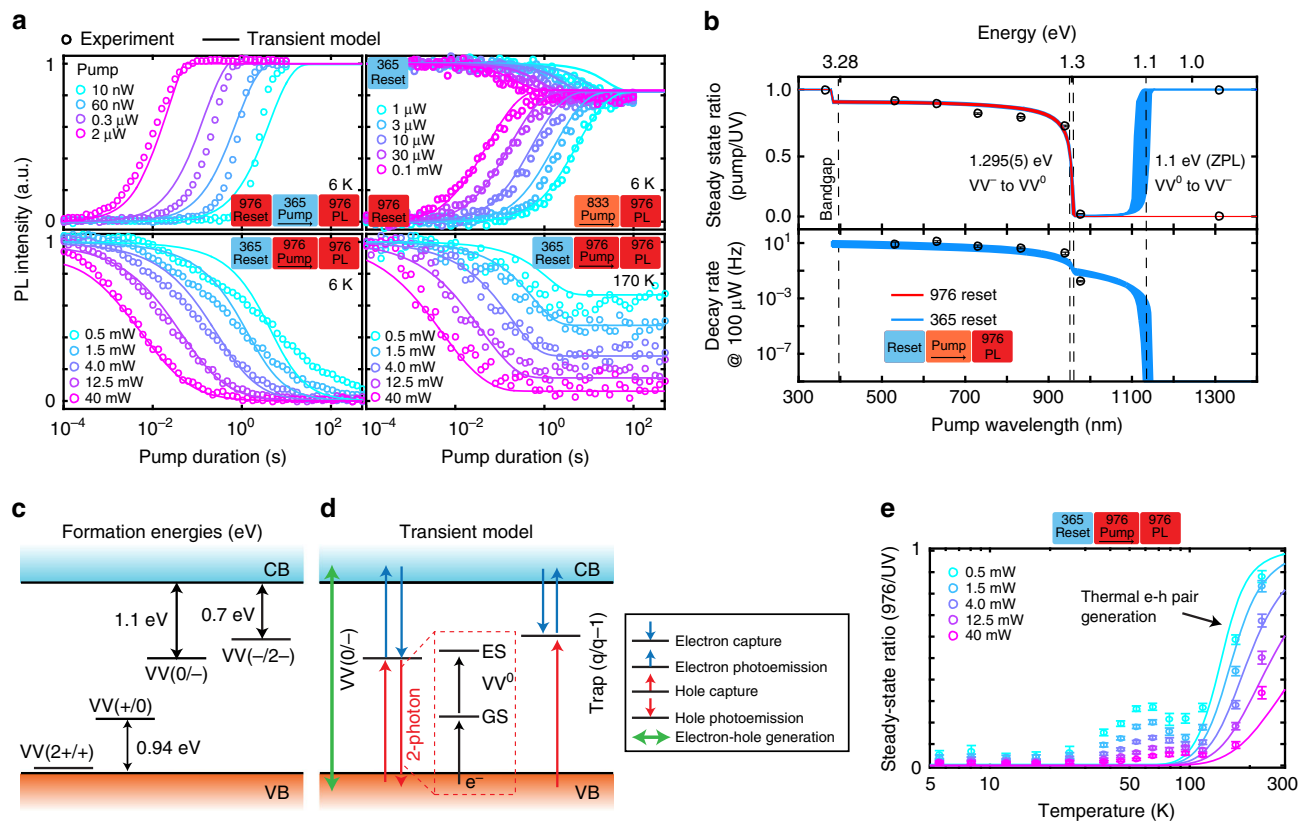


**Fig. 3** Photo-dynamics and modeling in neutral divacancies in 4H-SiC. The charge dynamics is probed using two and three color experiments, following a reset-pump-measure scheme. **a** Typical decay curves obtained under various reset/pump wavelength and temperatures. The fit (line) is obtained from the model given in **d**. **b** Top figure: ratio between pump and 365 nm steady-state PL intensities. Bottom figure: decay rates (normalized to 100  $\mu$ W at every pump wavelength) obtained by fitting the decays in **a** with a stretched exponential function (error bars are 95% confidence intervals from the fit). In blue, the sequence starts after 365 nm pumping, while in red, after 976 nm. The lines are given by the model in **d**, with the area corresponding to 95% confidence intervals. For 1310 nm, no significant decay was observed over 100 s, hence the steady-state values are given without error bars. **c** Formation energies of the divacancy in 4H-SiC, taken from<sup>20</sup>. **d** Model used for simulating all transients in **a**, **b**, **e**, including the  $VV^0$  and  $VV^-$  levels of the divacancy, as well as an unknown trap with two charge states. Processes included in the model are given in the legend. Hole photo-emission converting  $VV^0$  to  $VV^-$  involves a two-photon process, exciting  $VV^0$  from its ground state to its excited state, followed by excitation and capture of an electron from the valence band. **e** Temperature dependence of the steady state after 976 nm pumping (365 nm reset). Error bars are 95% confidence intervals from the decays' stretched exponential fit. Lines are given by the model in **d**, corresponding to thermal generation of electron-hole (e-h) pairs. The origin of the intermediate region between 30 and 100 K is unknown. Above 210 K, PL5 and PL6 signals become dominant, making the measurement unreliable as they are UV-insensitive

majority, are captured by the various deep defects, with  $VV^-$  being converted toward  $VV^0$  (high signal),  $V_{Si}^-$  toward  $V_{Si}^0$  (low signal), and possibly  $V_C^-$  toward  $V_C^+$  (high signal).

ESR measurements are often used to characterize the optimal annealing temperature for sample preparation. Changes in ESR intensity after sample annealing normally indicates variations in defect concentration, but can also be confused with a shift in the local Fermi level. After charge conversion, this second explanation is much less plausible. In Fig. 4c, the ESR intensity under best illumination condition (highest signal for each defect) was tracked for N,  $V_{Si}$ , and VV for different annealing temperatures. Between 1000 and 1400  $^{\circ}$ C, the ESR signal of  $V_{Si}$  and VV significantly drops, which can be related to the defects becoming mobile followed by creation of multi-vacancies such as  $V_C-V_{Si}-V_C$ <sup>38-41</sup>.

The ESR experiments indicate a strong relationship between VV and  $V_{Si}$ , as they are both affected by the 940–976 nm transition and by similar annealing temperatures. With  $V_{Si}^-$  being also a photo-active qubit of interest, we directly measure its PL by exciting the sample with 780 nm (Supplementary Fig. 1)<sup>5, 42</sup>. Three-pulse experiments for  $V_{Si}^-$  are shown in Fig. 5 with pumping using 365, 976 nm, as well as 780 nm as a replacement

for 940 nm which was impractical here. 365 nm pumping drastically decreases the  $V_{Si}^-$  intensity while both 976 and 780 nm convert back the charge state to  $V_{Si}^-$ .

These observations are consistent with the ESR experiments. Under 976 nm illumination, the  $V_{Si}$  PL signal recovers very slowly, with corresponding low ESR signal, and with little power dependence indicating competition between different carrier capture processes. In this case,  $VV^0$  emits holes by inefficient two-photon absorption, while N (and likely  $V_C$ ) emits electrons which will dominantly convert  $V_{Si}^0$  toward  $V_{Si}^-$  after capture. At 940 nm,  $VV^-$  also now emits electrons allowing for faster conversion to  $V_{Si}^-$ . At 780 nm, it is likely that conversion via capture is enhanced by direct photoionization of  $V_{Si}^0$  with (0/-) transition energy at  $E_v + 1.3-1.5$  eV (20, 43, reproduced in Supplementary Fig. 4). For completeness, the  $V_{Si}$  (-/2-) transition with a formation energy of  $E_c - 0.6-0.8$  eV is likely also excited at any wavelength below 976 nm, and therefore  $V_{Si}$  is more likely to be trapped in  $V_{Si}^-$  than in the 2- charge state. 780 nm illumination is therefore suitable for both  $V_{Si}^-$  PL excitation and  $V_{Si}^-$  charge stabilization.

The full VV/  $V_{Si}$  /N charge conversion picture under illumination is finally summarized in Fig. 6 for the three critical

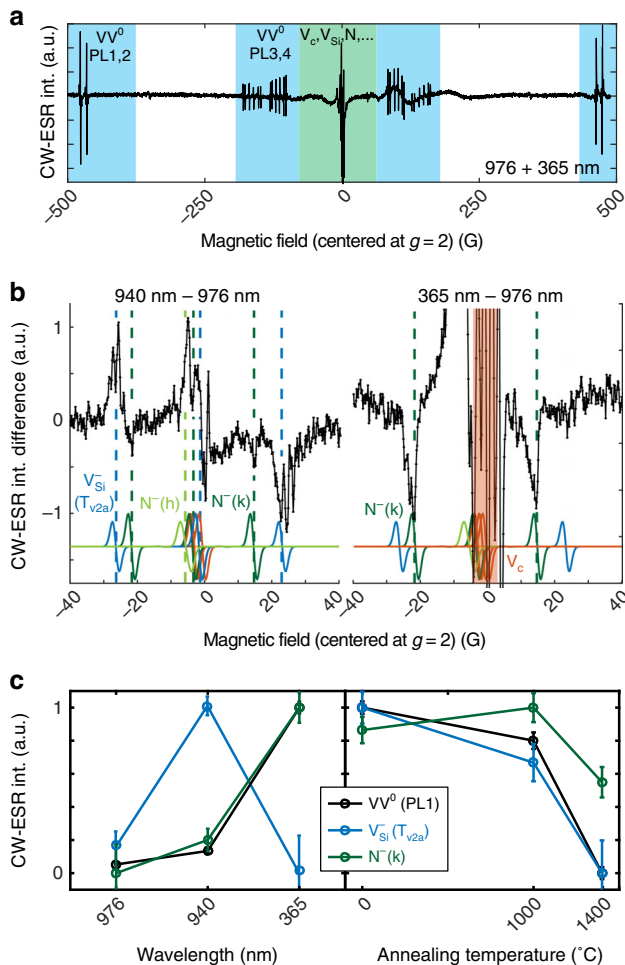


**Fig. 4** ESR at 15 K in semi-insulating 4H-SiC under illumination. **a** CW-ESR spectrum measured at 9.7 GHz, and centered around  $g \approx 2$  ( $\approx 3470$  G, aligned to the  $c$  axis). VV PL1-4 are highlighted in blue, while defects such as N,  $V_c$ , or  $V_{Si}$  are close to  $g \approx 2$  and highlighted in green. **b** Differential CW-ESR spectrum between either 940 nm and 976 nm excitation (left), or between 365 and 976 nm (right). Gaussian derivative lineshapes are simulated in color for known defects in 4H-SiC<sup>18</sup>. Their amplitudes only take into account transition probabilities, and not spin polarization or microwave saturation. **c** Normalized (per defect) CW-ESR intensity under 976, 940, and 365 nm (left) and for different annealing condition of the sample (right). For  $VV^0$ , 365 nm is combined with 976 nm for spin polarization (and obtain enough signal). For the annealing dependence, the intensity was fitted under the best illumination condition for each defect, that is the maximum signal in the left. Annealed samples were only used in this panel (**c**, right). Error bars are 95% confidence intervals from the fit

wavelengths explored in this work: 976, 940, and 365 nm.  $V_c$  was not taken into account due to lack of experimental measurements.

**Summary of charge dynamics.** Our overall summary of the charge conversion is as follows: (i) Under 365 nm excitation and electron-hole generation, N dominantly traps electrons toward  $N^-$ , while VV and  $V_{Si}$  capture the remaining holes to become  $VV^0$  and  $V_{Si}^0$ . (ii) Below but close to 940 nm in wavelength, VV chiefly emits electrons and ends up in  $VV^0$ , while  $V_{Si}$  captures those electrons to become  $V_{Si}^-$ . N will be in an intermediate charge state as it absorbs both electron and holes, as well as being photoionized. (iii) At wavelengths higher than 976 nm, VV is converted to  $VV^-$  by slow hole emission to the valence band

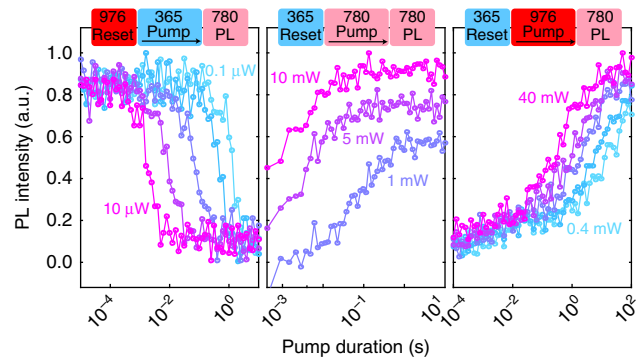


**Fig. 5** Photo-dynamics of  $V_{Si}^-$  at 6 K. Reset-pump-measure scheme similar to Fig. 3, but with 780 nm to excite PL in  $V_{Si}^-$  instead of 976 nm for  $VV^0$ . Each of the curves correspond to different pump powers (logarithmic increment for 365 and 976 nm). 365 nm reduces the PL intensity, likely from charge conversion to  $V_{Si}^-$ . Both 976 and 940 nm reinitialize VV toward its bright  $V_{Si}^-$  state, but with different rates and power dependence, indicating charge transfer with VV. Charge conversion was measured to be persistent without light on the experiment timescales

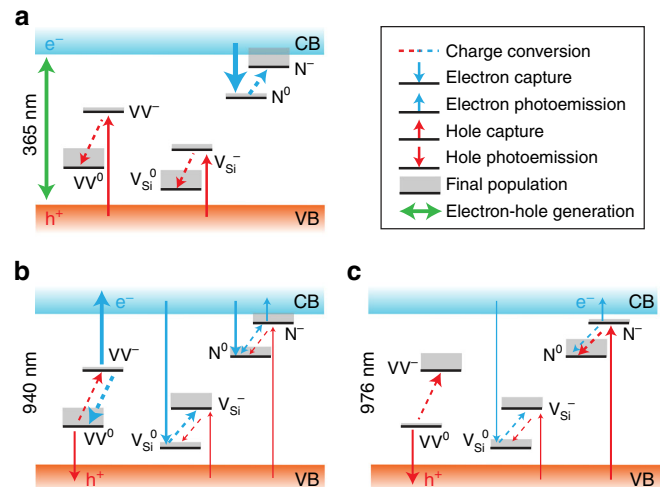


**Fig. 6** Summary of charge transfer in semi-insulating 4H-SiC under various illumination conditions. Strong transitions are shown by thicker arrows, and the steady-state population after illumination is approximately represented by the gray area over each state. **a** Above-bandgap excitation and electron-hole generation. **b** Excitation above the  $VV^-$  photoionization transition ( $-1.3$  eV). **c** Excitation below the  $VV^-$  photoionization transition, but above  $VV^0$  two-photon absorption

through a two-photon process; N is still photoionized resulting in  $N^0$  while  $V_{Si}$  capture both holes and electrons for a slow conversion toward  $V_{Si}^-$ .

The charge conversion and transfer mechanisms presented throughout this work should remain valid in most semi-insulating materials, where defects are in comparable concentrations. For n- or p-doped materials, impurities can of course still be photoionized, however, electron-hole generation with above-bandgap light will likely set the local Fermi level to a different equilibrium than what is seen here.

**Toward applications in charge patterning.** To complete this study, we turn toward applications using our ability to control the VV charge state. In recent experiments in diamond<sup>28</sup>, optical conversion between the  $NV^-$  and  $NV^0$  states was used to demonstrate the possibility of information storage by 3D

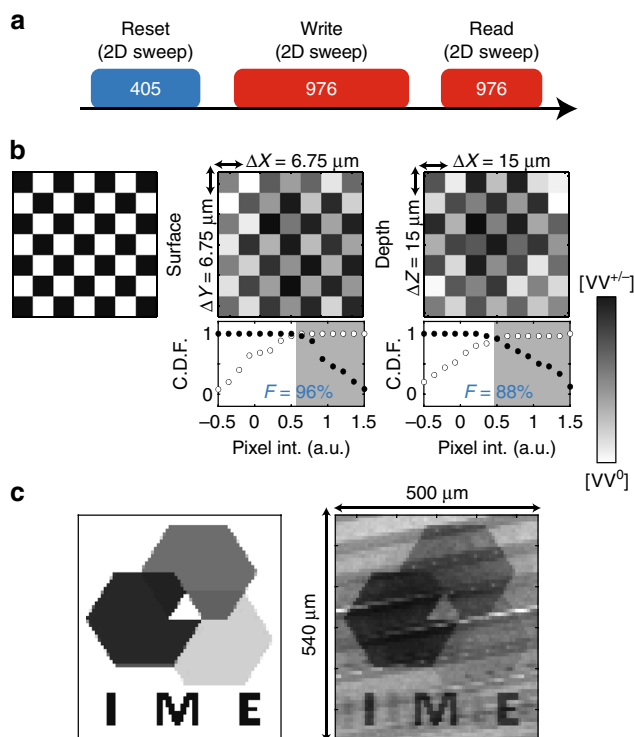


**Fig. 7** Spatial and amplitude control of the divacancy charge conversion. **a** Imaging sequence for **b**, **c**, with three sequential 2D sweeps: (1) Reset to high  $VV^0$  concentration using 405 nm. (2) Write using 976 nm with varying duration for charge conversion back to a desired lower  $VV^0$  concentration. (3) Read with a fast 976 nm pulse. **b** Pixel test of spatial control with, from left to right, the original pattern, the measured pattern in the X–Y plane (parallel to the sample surface) and the measured pattern in the X–Z plane (orthogonal to the sample surface). For X–Z, the intensity is normalized to the PL collection efficiency across the sample depth. Below each image, the corresponding cumulative distribution function (C.D.F.) is plotted from cumulative binning of the pixels according to their intensity (int.) and expected color (black/white dots for black/white pixels). The fidelity  $F$  is defined as  $1 - P(b|w) - P(w|b)$ , where  $P(i|j)$  is the probability of measuring  $i$  expecting  $j$ , where  $i, j = \text{black (b), white (w)}$ , and the expected color is given by the background color in the plot<sup>50</sup>. **c** Amplitude control of the charge conversion using a gray scale image (left: original image, right: experiment)

patterning of the charge state. Because data can be both encoded in 3D, as well as a gradient of charge conversion, high storage densities can theoretically be achieved. We present a similar demonstration of charge patterning in 4H-SiC, and though our experiments are realized at 6 K, offer the potential for storage across entire wafers compared to diamond. The  $VV$  charge conversion works relatively well up to 150–200 K, and may possibly be extended to room temperature with the adequate choice of material (dominant dopant or impurity concentration).

The patterning scheme is presented in Fig. 7a with: a UV (405 nm) pulse to initialize the sample toward  $VV^0$ , a write pulse with 976 nm to selectively obtain  $VV^-$  (or possibly  $VV^+$ ), and finally a short read pulse using 976 nm. The measurement pulse here weakly erases the information due to undesired charge conversion, which is the main limitation to this technique. In Fig. 7b, we test the spatial resolution of our setup by patterning a checkerboard design (left) where each square is a single pixel. This is realized first parallel to the sample plane (middle) and then in depth, orthogonal to the sample plane (right). Finally, for each pixel, we allow control over the amount of charge conversion,

increasing the density of information that can be locally stored. This is demonstrated in Fig. 7c by patterning a  $500 \times 540 \mu\text{m}$  gray scale image parallel to the sample surface.

## Discussion

In this work, we have systematically investigated the charge properties of divacancies in semi-insulating 4H-SiC, as well as other relevant defects, such as  $V_{\text{Si}}$  and N. Through optical excitation with wavelengths spanning from 365 to 1310 nm,  $VV$  was found to be stable in either its bright (neutral) or dark (negative or positive) charge configuration. The photoionization energy required to obtain the bright  $VV^0$  charge state was fitted to be around 1.3 eV, while below in energy two-photon ionization most likely converts  $VV$  to  $VV^-$ . As a consequence, the commonly used 976 nm (below 1.3 eV) excitation is found to be detrimental for PL measurements. Considering the maximum of the phonon sideband of  $VV^0$ , an excitation wavelength around 900–940 nm would be optimal, with commercial lasers readily available in this region. Above-bandgap excitation efficiently reshuffles the charge states of all defects, turning  $VV$  bright ( $VV^0$ ) and  $V_{\text{Si}}$  dark (possibly  $V_{\text{Si}}^0$ ).

While all the results here were realized in ensembles of defects, they should be equally applicable to single defects in similar SiC materials. A possible major difference may arise from the usually lower background impurity concentration required for single defect samples, which would change the charge dynamics and optical conversion. Similar to the NV center in diamond<sup>25, 44</sup>, the appropriate wavelength could reduce blinking due to transient charge conversion of single defects and increase their photoluminescence count rate.

Overall, taking into account multiple impurities was necessary to obtain a complete picture of charge effects in the SiC samples; such considerations are crucial for tuning wafer growth techniques, samples with implanted layers, surface impurities or for devices with complex electric potentials. Finally, we confirmed that these optical charge conversions drastically improve the PL intensity and do not measurably impact the spin properties (ODMR, coherence). Combined with recent studies<sup>10, 45</sup> characterizing the spin and optical properties of  $VV$  or  $V_{\text{Si}}$  in 4H and 3C-SiC, this work on charge conversion/stabilization helps to complete the suite of techniques and technologies realized in NV centers in diamond for use in SiC, while allowing for novel applications such as optically controlling the charge of spins in electronic devices realized in SiC. This study will also be relevant to spin-to-charge conversion in SiC, though further work is necessary.

## Methods

**Samples.** All measurements were performed on commercially available high-purity semi-insulating 4H-SiC diced wafers purchased from Cree<sup>32</sup>, and using a scanning ODMR microscopy setup. Similar wafers have been used in other studies, with measured defect concentrations of N,  $VV$ ,  $V_{\text{Si}}$  all in the order of  $10^{14}$ – $10^{16} \text{ cm}^{-3}$ <sup>32, 46, 47</sup>. For the implanted sample, a high energy carbon implant ( $[^{12}\text{C}] = 10^{13} \text{ cm}^{-2}$ , 190 keV, 900 °C anneal for 40 min) was used, resulting in a calculated (SRIM software) 500 nm thick layer of divacancies. For ODMR, the samples are fixed to a printed circuit board patterned with a coplanar waveguide for magnetic resonance, and mounted in a closed-cycle cryostat cooled down to 5–6 K (unless otherwise mentioned). PL, ODMR, and ESR experiments were all realized on ensembles of defects.

**PL and ODMR set-ups.** For  $VV^0$ , the sample is excited with a 976 nm diode laser (40 mW at sample, focused with a  $\times 50$  IR objective) and PL is measured with an InGaAs detector (1000–1300 nm after filtering). For  $V_{\text{Si}}^-$ , the sample is excited with a 780 nm diode laser (10 mW at sample) and PL is measured with a Si detector (850–950 nm after filtering, allowing simultaneous  $VV^0$  PL recording). Simplified schematics for the PL/ODMR set-ups are given in Supplementary Fig. 1. All given optical powers were measured at the sample. Excitation spectra are recorded by inserting a monochromator immediately after a 100 W Xe white light source in the optical set-up. Emission spectra or measurements at selective zero-phonon lines

(ZPL) are recorded by inserting a monochromator before the detector. For the wavelength dependence, a set of laser diodes were successively collimated into a 300  $\mu\text{m}$  multi-mode fiber and re-emitted into free space so as to ensure a constant spot position on the sample. It should also be noted there is no significant PL contribution from 405 or 365 nm illumination alone.

**Transients and modeling.** The three-pulse scheme used for the photo-dynamics requires careful choice of the 976 nm measurement pulse duration (0.1 ms) as it is necessary for exciting PL but can also change the charge state of VV. A long pulse would effectively smooth the decays and prevent good fitting at short times. The experimental decay rates and steady states are obtained from fitting with a stretched exponential function, with separate fitting parameters for each power, wavelength and temperature dependence. The actual decay curves are shown in Supplementary Fig. 3, and all simulated lines in Fig. 3 are from the rate-equation model. All details on this model are given in Supplementary Note 1, regarding e.g., simulation of the wavelength dependence (Grimmeiss model for deep trap<sup>48</sup>) and the exact rate equations.

In total, 12 parameters are used for a simultaneous fit over a set of 70 decays curves, with the simulation results shown by the lines in Fig. 3a, b, e. Looking at the decays in Fig. 3a, the fits are in excellent agreement in certain ranges (833 nm pumping) but do not account for all the charge dynamics as seen in the left figures. For 365 nm pumping, electron-hole pair generation dominates over all photoionization processes, and the free carrier concentration is determined by the recombination with all involved traps, not just VV. Hence for such a simple model, large discrepancies are expected. In addition, the simulation strictly considers a single defect while measuring an ensemble can easily smooth features in the decays, e.g., due to local variations in strain, charge, light intensity, etc.

**Electron spin resonance.** ESR experiments were realized on a X-band (dielectric resonator, 5 mm internal diameter) ELEXSYS E580 Bruker spectrometer at 15 K. In the differential experiments presented in Fig. 4, one important issue is the simultaneous effect of illumination on both spin (polarization, relaxation) and charge properties, and hence on the ESR intensity. The results presented may convolute both aspects, unlike the PL experiments which are clearly related to the charge state. Turning the lasers on and off would avoid this concern, however the signal was then simply too weak to obtain any information on  $N$ ,  $V_C$  or  $V_{Si}$ . The 940 and 976 nm excitation lasers are sufficiently close in energy to limit most effects but those related to the sharp photoionization transition in VV. In addition, these wavelengths are both in the VV absorption sideband, but close enough to see no appreciable differences in spin polarization due to inter-system crossing mechanisms. Similarly, they are also above the longest ZPL wavelength of  $V_{Si}^-$  (917 nm<sup>5</sup>), preventing any spin polarization.

**Data availability.** The data that support the findings of this study are available upon request to the corresponding author.

Received: 26 May 2017 Accepted: 30 October 2017

Published online: 30 November 2017

## References

- Waldherr, G. et al. Quantum error correction in a solid-state hybrid spin register. *Nature* **506**, 204–207 (2014).
- Maze, J. R. et al. Nanoscale magnetic sensing with an individual electronic spin in diamond. *Nature* **455**, 644–647 (2008).
- Toyli, D. M., de las Casas, C. F., Christle, D. J., Dobrovitski, V. V. & Awschalom, D. D. Fluorescence thermometry enhanced by the quantum coherence of single spins in diamond. *Proc. Natl Acad. Sci. USA* **110**, 8417–8421 (2013).
- Kucsko, G. et al. Nanometre-scale thermometry in a living cell. *Nature* **500**, 54–58 (2013).
- Baranov, P. G. et al. Silicon vacancy in SiC as a promising quantum system for single-defect and single-photon spectroscopy. *Phys. Rev. B* **83**, 125203 (2011).
- Koehl, W. F., Buckley, B. B., Heremans, F. J., Calusine, G. & Awschalom, D. D. Room temperature coherent control of defect spin qubits in silicon carbide. *Nature* **479**, 84–87 (2011).
- Kraus, H. et al. Room-temperature quantum microwave emitters based on spin defects in silicon carbide. *Nat. Phys.* **10**, 157–162 (2013).
- Christle, D. J. et al. Isolated electron spins in silicon carbide with millisecond coherence times. *Nat. Mater.* **14**, 160–163 (2014).
- Widmann, M. et al. Coherent control of single spins in silicon carbide at room temperature. *Nat. Mater.* **14**, 164–168 (2014).
- Christle, D. J. et al. Isolated spin qubits in sic with a high-fidelity infrared spin-to-photon interface. *Phys. Rev. X* **7**, 021046 (2017).
- Janzén, E. et al. The silicon vacancy in SiC. *Phys. B: Condens. Matter* **404**, 4354–4358 (2009).

- Torpo, L., Staab, T. & Nieminen, R. Divacancy in 3C- and 4H-SiC: an extremely stable defect. *Phys. Rev. B* **65**, 1–10 (2002).
- Son, N. T. et al. Divacancy in 4H-SiC. *Phys. Rev. Lett.* **96**, 055501 (2006).
- Falk, A. L. et al. Polytype control of spin qubits in silicon carbide. *Nat. Commun.* **4**, 1819 (2013).
- Booker, I. D. et al. Carrier lifetime controlling defects Z 1/2 and RB1 in standard and chlorinated chemistry grown 4H-SiC. *Cryst. Growth Design* **14**, 4104–4110 (2014).
- Booker, I. D. et al. Donor and double-donor transitions of the carbon vacancy related EH 67 deep level in 4H-SiC. *J. Appl. Phys.* **119**, 235703 (2016).
- Matsumoto, T., Poluektov, O. G., Schmidt, J., Mokhov, E. N. & Baranov, P. G. Electronic structure of the shallow boron acceptor in 6H-SiC:ma pulsed EPR/ENDOR study at 95 GHz. *Phys. Rev. B* **55**, 2219–2229 (1997).
- Isoya, J. et al. EPR identification of intrinsic defects in SiC. *Phys. Status Solidi (b)* **245**, 1298–1314 (2008).
- Gali, A. Excitation spectrum of point defects in semiconductors studied by time-dependent density functional theory. *J. Mater. Res.* **27**, 897–909 (2012).
- Gordon, L., Janotti, A. & Van de Walle, C. G. Defects as qubits in 3C and 4H-SiC. *Phys. Rev. B* **92**, 045208 (2015).
- Weber, J. R. et al. Defects in SiC for quantum computing. *J. Appl. Phys.* **109**, 102417 (2011).
- Umeda, T. et al. EPR and theoretical studies of negatively charged carbon vacancy in 4HSiC. *Phys. Rev. B* **71**, 193202 (2005).
- Son, N. T. et al. Negative-system of carbon vacancy in 4H-SiC. *Phys. Rev. Lett.* **109**, 187603 (2012).
- Umeda, T., Morishita, N., Ohshima, T., Itoh, H. & Isoya, J. Photo-EPR study of vacancy-type defects in irradiated n-type 4H-SiC. *Mater. Sci. Forum* **600–603**, 409–412 (2009).
- Aslam, N., Waldherr, G., Neumann, P., Jelezko, F. & Wrachtrup, J. Photo-induced ionization dynamics of the nitrogen vacancy defect in diamond investigated by single-shot charge state detection. *New. J. Phys.* **15**, 013064 (2013).
- Siyushev, P. et al. Optically controlled switching of the charge state of a single nitrogen-vacancy center in diamond at cryogenic temperatures. *Phys. Rev. Lett.* **110**, 167402 (2013).
- Bassett, L. C., Heremans, F. J., Yale, C. G., Buckley, B. B. & Awschalom, D. D. Electrical tuning of single nitrogen-vacancy center optical transitions enhanced by photoinduced fields. *Phys. Rev. Lett.* **107**, 266403 (2011).
- Dhomkar, S., Henshaw, J., Jayakumar, H. & Meriles, C. A. Long-term data storage in diamond. *Sci. Adv.* **2**, e1600911–e1600911 (2016).
- Han, K. Y., Kim, S. K., Eggeling, C. & Hell, S. W. Metastable dark states enable ground state depletion microscopy of nitrogen vacancy centers in diamond with diffraction-unlimited resolution. *Nano Lett.* **10**, 3199–3203 (2010).
- Chen, X. et al. Subdiffraction optical manipulation of the charge state of nitrogen vacancy center in diamond. *Light: Sci. Appl.* **4**, e230 (2015).
- Doherty, M. W. et al. Towards a room-temperature spin quantum bus in diamond via electron photoionization, transport, and capture. *Phys. Rev. X* **6**, 041035 (2016).
- Jenny, J. R. et al. Development of large diameter high-purity semi-insulating 4H-SiC wafers for microwave devices. *Mater. Sci. Forum* **457–460**, 35–40 (2004).
- Zargaleh, S. A. et al. Evidence for near-infrared photoluminescence of nitrogen vacancy centers in 4H-SiC. *Phys. Rev. B* **94**, 060102 (2016).
- Seo, H. et al. Quantum decoherence dynamics of divacancy spins in silicon carbide. *Nat. Commun.* **7**, 12935 (2016).
- Tyryshkin, A. M. et al. Electron spin coherence exceeding seconds in high-purity silicon. *Nat. Mater.* **11**, 143–147 (2011).
- Cs6r6, A., von Bardeleben, H. J., Cantin, J. L. & Gali, A. Characterization and formation of NV centers in 3C, 4H and 6H SiC: An ab initio study. *Phys. Rev. B* **96**, 085204 (2017).
- Golter, D. A. & Lai, C. W. Optical switching of defect charge states in 4H-SiC. *Sci. Rep.* **7**, 13406 (2017).
- Gerstmann, U., Rauls, E., Frauenheim, T. & Overhof, H. Formation and annealing of nitrogen-related complexes in SiC. *Phys. Rev. B* **67**, 205202 (2003).
- Zolnai, Z., Son, N. T., Hallin, C. & Janzén, E. Annealing behavior of the carbon vacancy in electron-irradiated 4H-SiC. *J. Appl. Phys.* **96**, 2406–2408 (2004).
- Schmid, F. et al. Deactivation of nitrogen donors in silicon carbide. *Phys. Rev. B* **74**, 245212 (2006).
- Carlos, W. E., Garc6s, N. Y., Glaser, E. R. & Fanton, M. A. Annealing of multivacancy defects in 4HSiC. *Phys. Rev. B* **74**, 235201 (2006).
- Embley, J. S. et al. Electron spin coherence of silicon vacancies in proton-irradiated 4 H -SiC. *Phys. Rev. B* **95**, 045206 (2017).
- Hornos, T., Gali, A. & Svensson, B. G. Large-scale electronic structure calculations of vacancies in 4H-SiC using the hybrid-scuseria-ernzerhof screened hybrid density functional. *Mater. Sci. Forum* **679–680**, 261–264 (2011).



44. Fu, K.-M. C. M. C., Santori, C., Barclay, P. E. & Beausoleil, R. G. Conversion of neutral nitrogen-vacancy centers to negatively charged nitrogen-vacancy centers through selective oxidation. *Appl. Phys. Lett.* **96**, 121907 (2010).
45. Fuchs, F. et al. Engineering near-infrared single-photon emitters with optically active spins in ultrapure silicon carbide. *Nat. Commun.* **6**, 7578 (2015).
46. Son, N. T., Carlsson, P., ul Hassan, J., Magnusson, B. & Janzén, E. Defects and carrier compensation in semi-insulating 4H-SiC substrates. *Phys. Rev. B* **75**, 155204 (2007).
47. Chandrashekar, M. V. S. et al. High purity semi-insulating 4H-SiC epitaxial layers by defect-competition epitaxy: controlling Si vacancies. *Appl. Phys. Express* **5**, 025502 (2012).
48. Grimmeiss, H. G. & Ledebro, L. A. Photo-ionization of deep impurity levels in semiconductors with non-parabolic bands. *J. Phys. C: Solid State Phys.* **8**, 2615–2626 (1975).
49. Galeckas, A., Grivickas, P., Grivickas, V., Bikbajevs, V. & Linnros, J. Temperature dependence of the absorption coefficient in 4H- and 6H-silicon carbide at 355 nm laser Pumping wavelength. *Phys. Status Solidi (a)* **191**, 613–620 (2002).
50. Morello, A. et al. Single-shot readout of an electron spin in silicon. *Nature* **467**, 687–691 (2010).

## Acknowledgements

We thank Ádám Gali, Hosung Seo, Alexandre Bourassa and David Christle for discussions. This work was supported by the ARL OSD QSEP program and the NSF EFRI 1641099 grant. G.W. acknowledges support from the University of Chicago/Advanced Institute for Materials Research (AIMR) Joint Research Center. A.L.Y., F.J.H., and D.D.A. were supported by the US Department of Energy, Office of Science, Basic Energy Sciences, Materials Science and Engineering Division at Argonne National Laboratory. J.N. and O.G.P. were supported by the U.S. Department of Energy, Office of Science, Office of Basic Energy Sciences, Division of Chemical Sciences, Biosciences and Geosciences under Contract DE-AC02-06CH11357 at Argonne National Laboratory. C.P.A. was supported by the Department of Defense (DoD) through the National Defense Science and Engineering Graduate Fellowship (NDSEG) Program.

## Author contributions

G.W., C.P.A., and A.L.Y. performed the optical experiments. G.W., J.N., O.G.P., and F.J.H. performed the electron spin resonance experiments. A.L.Y., S.J.W., and C.P.A., processed the annealed and implanted samples. D.D.A. advised and coordinated all efforts. All the authors contributed to analysis of the data, discussions and the production of the manuscript.

## Additional information

**Supplementary Information** accompanies this paper at doi:10.1038/s41467-017-01993-4.

**Competing interests:** The authors declare no competing financial interests.

**Reprints and permission** information is available online at <http://npg.nature.com/reprintsandpermissions/>

**Publisher's note:** Springer Nature remains neutral with regard to jurisdictional claims in published maps and institutional affiliations.



**Open Access** This article is licensed under a Creative Commons Attribution 4.0 International License, which permits use, sharing, adaptation, distribution and reproduction in any medium or format, as long as you give appropriate credit to the original author(s) and the source, provide a link to the Creative Commons license, and indicate if changes were made. The images or other third party material in this article are included in the article's Creative Commons license, unless indicated otherwise in a credit line to the material. If material is not included in the article's Creative Commons license and your intended use is not permitted by statutory regulation or exceeds the permitted use, you will need to obtain permission directly from the copyright holder. To view a copy of this license, visit <http://creativecommons.org/licenses/by/4.0/>.

© The Author(s) 2017